Science Advances

AAAS

advances.sciencemag.org/cgi/content/full/4/3/eaaq0118/DC1

Supplementary Materials for

Surface-agnostic highly stretchable and bendable conductive MXene multilayers

Hyosung An, Touseef Habib, Smit Shah, Huili Gao, Miladin Radovic, Micah J. Green, Jodie L. Lutkenhaus

Published 9 March 2018, *Sci. Adv.* **4**, eaaq0118 (2018)
DOI: 10.1126/sciadv.aaq0118

The PDF file includes:

- table S1. Atomic composition at the surface of cast MXene sheets, $(PDAC/MXene)_{20}$ multilayer terminated with MXene, and $(PDAC/MXene)_{20.5}$ multilayer terminated with PDAC from XPS survey spectra (fig. S8).
- table S2. Characteristics of flexible MXene-based films or coatings.
- table S3. Characteristics of reported bendable conductors.
- table S4. Characteristics of reported stretchable conductors.
- Legends for movies S1 to S10
- References (*29–61*)

Other Supplementary Material for this manuscript includes the following:
(available at advances.sciencemag.org/cgi/content/full/4/3/eaaq0118/DC1)

- movie S1 (.mov format). A nylon fiber coated with a MXene multilayer, showing conductive properties.
- movie S2 (.mov format). An MXene multilayer on PET lights up a white LED under folding.
- movie S3 (.mov format). Cyclic bending of a MXene multilayer on PET shows rapid and reversible response.
- movie S4 (.mov format). An MXene multilayer on PET detects bending deformations.
- movie S5 (.mov format). A kirigami MXene multilayer on PET detects stretching deformations.
- movie S6 (.mov format). A kirigami pattern allows MXene multilayer–coated PET to be stretchable.
- movie S7 (.mov format). An MXene multilayer on PDMS detects stretching deformations.
- movie S8 (.mov format). An MXene multilayer on PDMS detects a twisting deformation.
- movie S9 (.mov format). A patterned multilayer strain sensor detects various degrees of bending (0° to 40°) with rapid response.
- movie S10 (.mov format). A topographic scanner was fabricated using a patterned MXene multilayer–coated PET film.

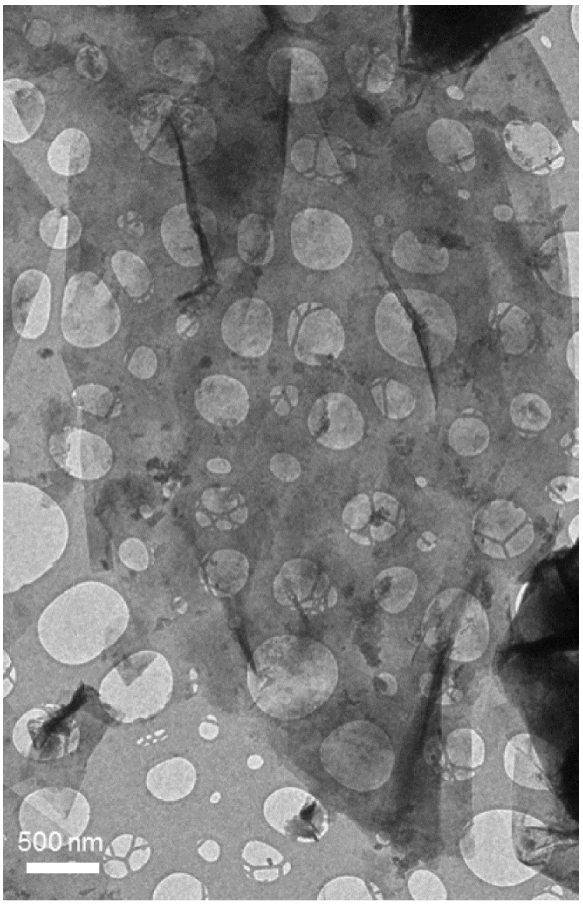

fig. S1. TEM image of a Ti_3C_2 MXene nanosheet on a perforated carbon grid. The nanosheet is several microns wide.

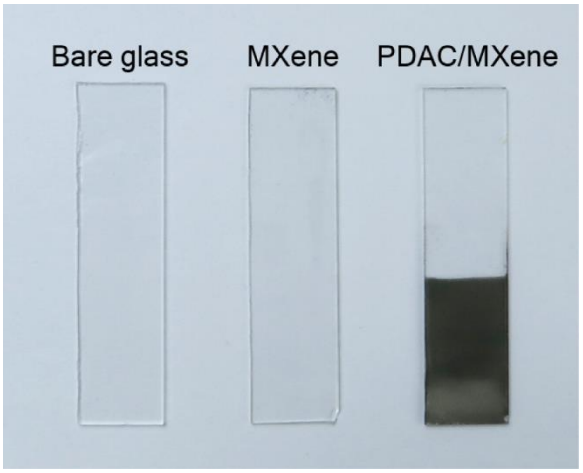

fig. S2. Digital images of (left) bare glass, (middle) the result of LbL assembly using only MXene sheets (without PDAC solution), and (right) 10-layer-pair MXene/PDAC multilayer coating. There was no observable growth for the LbL assembly with only the MXene sheet dispersion.

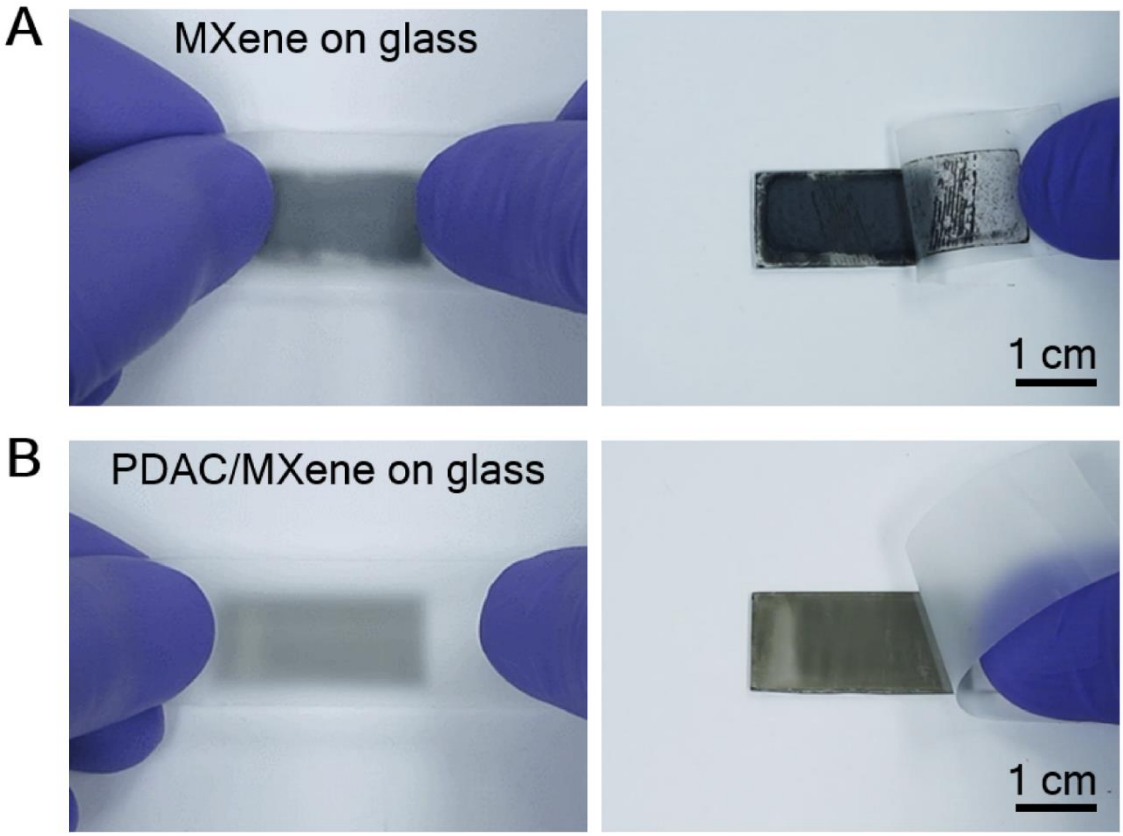

fig. S3. Adhesion testing with tape. Digital images of adhesion testing with 3M Scotch tape on (A) drop-cast MXene sheets and (B) a MXene-based multilayer coating on glass substrates. The adhesion tests were carried out by strongly attaching the tape, and subsequently peeling it off. The drop-cast MXene sheets showed very poor adhesion, and the multilayer showed excellent adhesion.

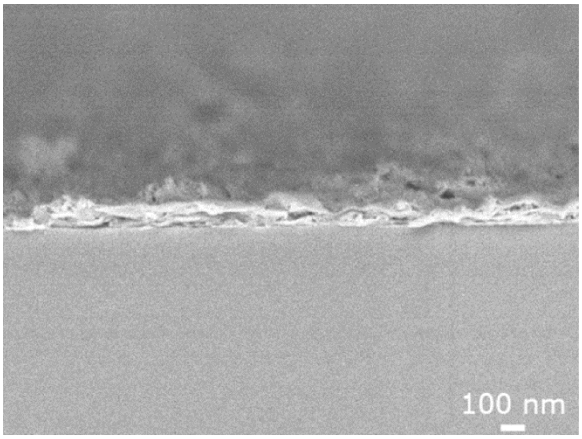

fig. S4. A cross-sectional SEM image of the MXene multilayer prepared by spray-assisted LbL assembly on glass.

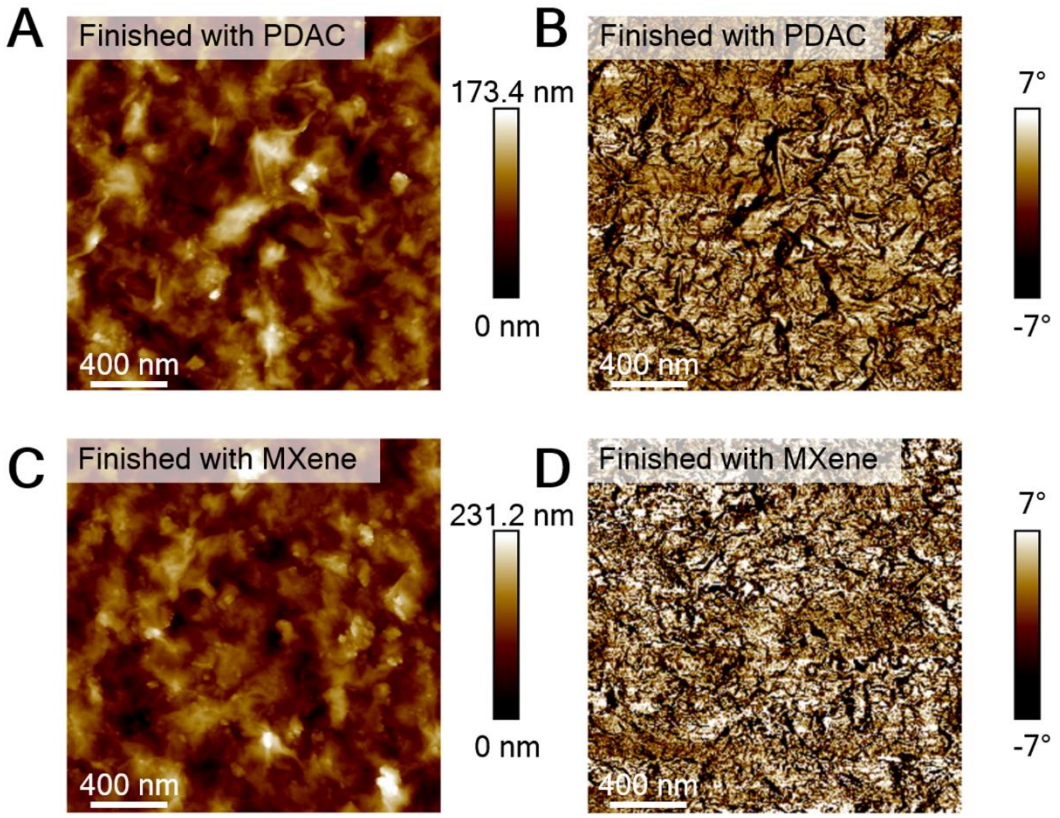

fig. S5. AFM images of PDAC/MXene multilayers. AFM height and phase images (2 μm × 2 μm) of (**A**, **B**) a $(PDAC/MXene)_{50.5}$ LbL film finished with PDAC and (**C**, **D**) a $(PDAC/MXene)_{50}$ LbL film finished with MXene. Figure S5 shows tapping-mode AFM height and phase images of the MXene multilayer on glass. Both multilayers that were finished with MXene as the last layer and PDAC as the last layer possessed similar surface morphologies. RMS roughness values measured by profilometry of PDAC on top (25 ± 2 nm) and MXene on top (29 ± 3 nm) coatings were similar. In the AFM phase images (fig. S5B and S5D), the MXene-finished multilayer showed a higher phase angle (brighter color) than the PDAC-finished multilayer because MXene sheets are more rigid. The subscripts 50 and 50.5 refer to the number of layer pairs.

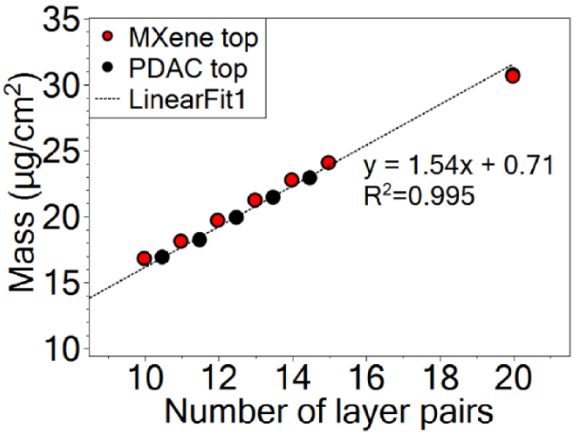

fig. S6. Thickness of the multilayers as a function of the number of layer pairs. Mass change was measured using QCM and the Sauerbrey equation. Average increases in mass for PDAC and MXene were 10.0 wt% and 90.0 wt%, respectively.

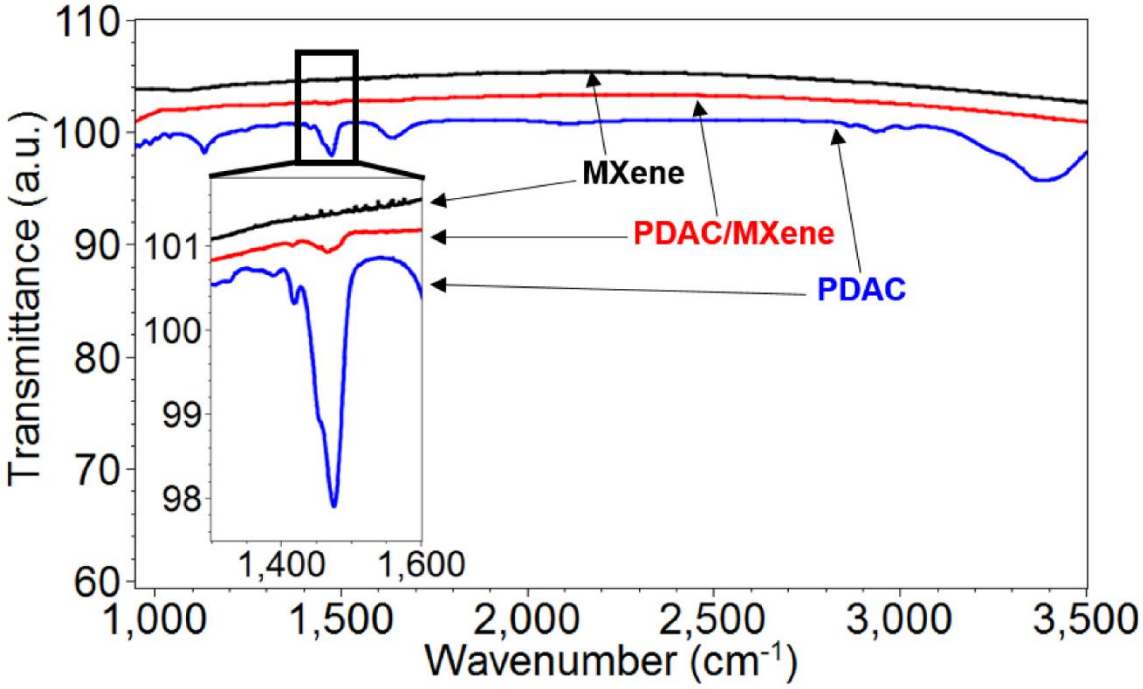

fig. S7. ATR-FTIR spectra of MXene, PDAC, and 20-layer-pair MXene multilayer coating. For the multilayer, a peak appeared at 1467 cm^{-1} (CH_2 bending), indicating the presence of PDAC (*29*).

MXene

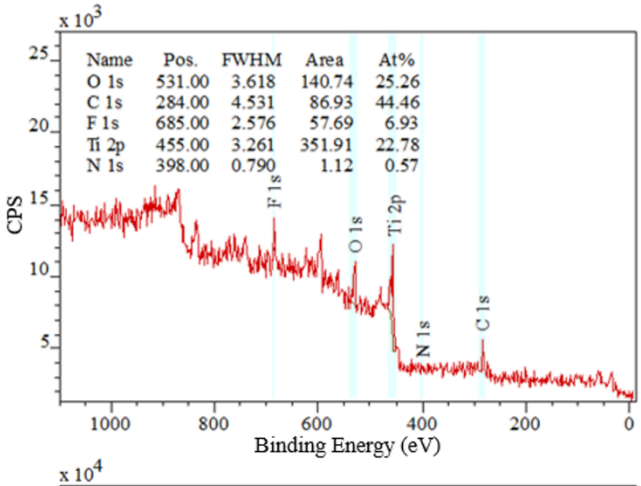

$(PDAC/MXene)_{20}$ LbL film finished with Mxene

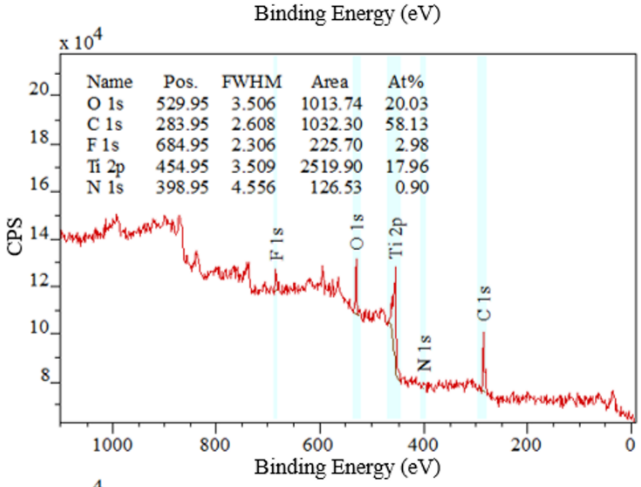

$(PDAC/MXene)_{20.5}$ LbL film finished with PDAC

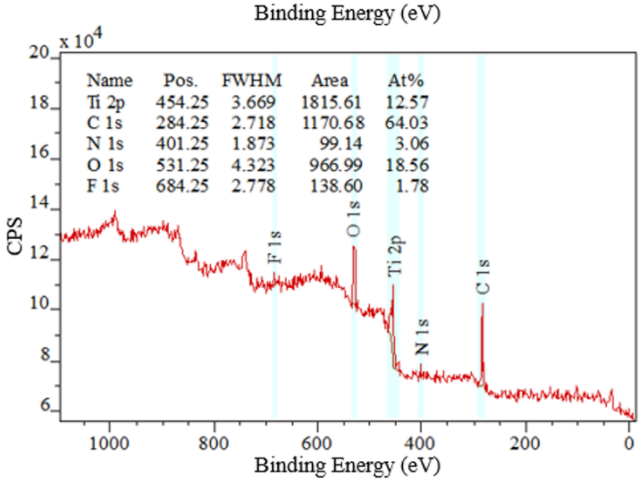

fig. S8. XPS survey spectra of MXene, $(PDAC/MXene)_{20}$ multilayer finished with MXene, and $(PDAC/MXene)_{20.5}$ multilayer finished with PDAC.

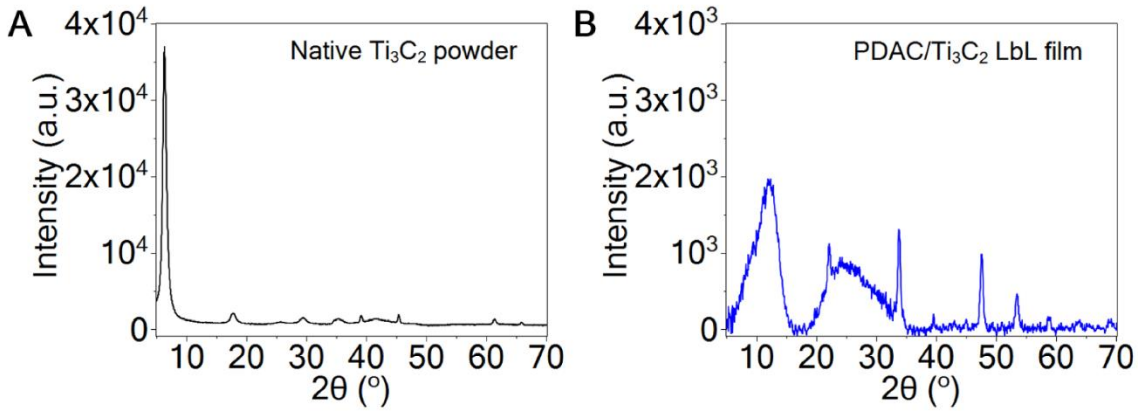

fig. S9. XRD of MXene powder and multilayer. XRD of (**A**) freeze-dried Ti_3C_2 MXene powder and (**B**) a PDAC/MXene LbL film (MXene multilayer) on glass.

Figure S9 shows XRD plots of freeze-dried Ti_3C_2 MXene nanosheets and a MXene multilayer coating prepared on glass. In fig. S9A, the peak at around 7˚ corresponds to MXene Ti_3C_2 nanosheets (as distinct from the parent MAX phase), in agreement with prior studies (*19*). This peak shifted to 11˚ and broadened significantly in the multilayer (fig. S9B).

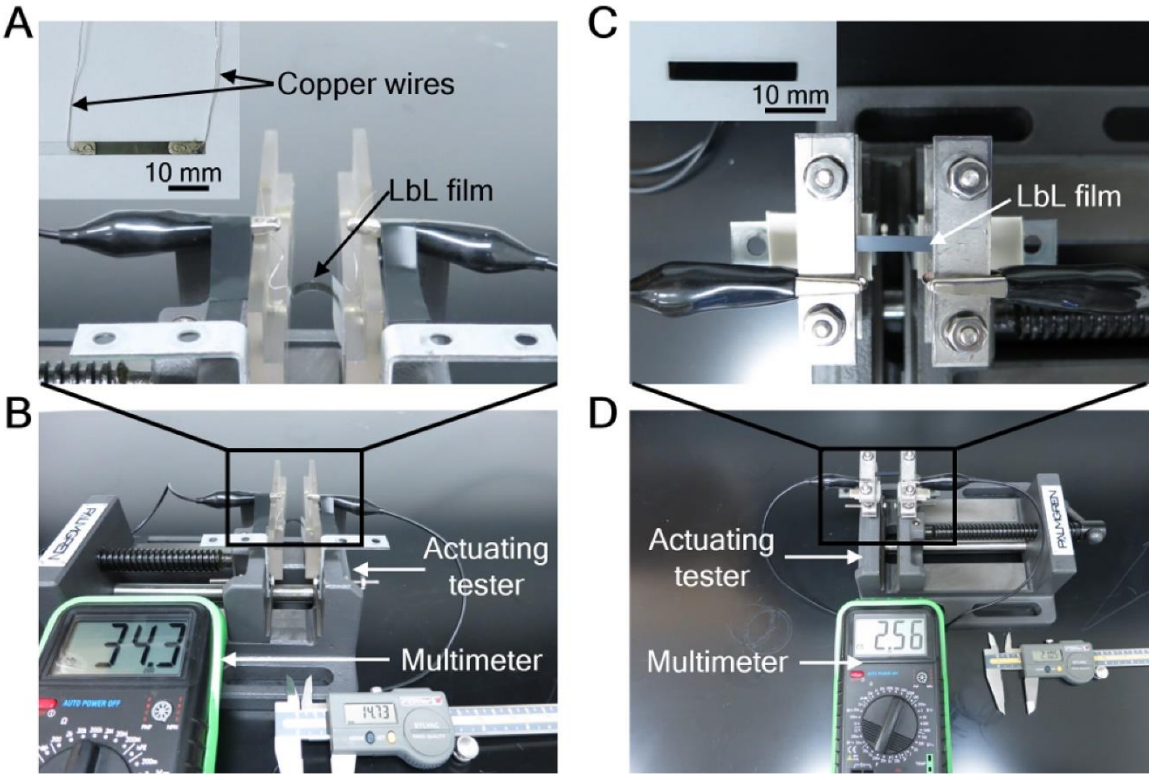

fig. S10. Digital images of MXene multilayers bending and stretching. Photographs of (**A**, **B**) bending of the MXene multilayer on PET (inset of A) and (**C**, **D**) stretching of the MXene multilayer on PDMS (inset of C). For bending, copper wires were connected to both ends of the multilayer using silver paste.

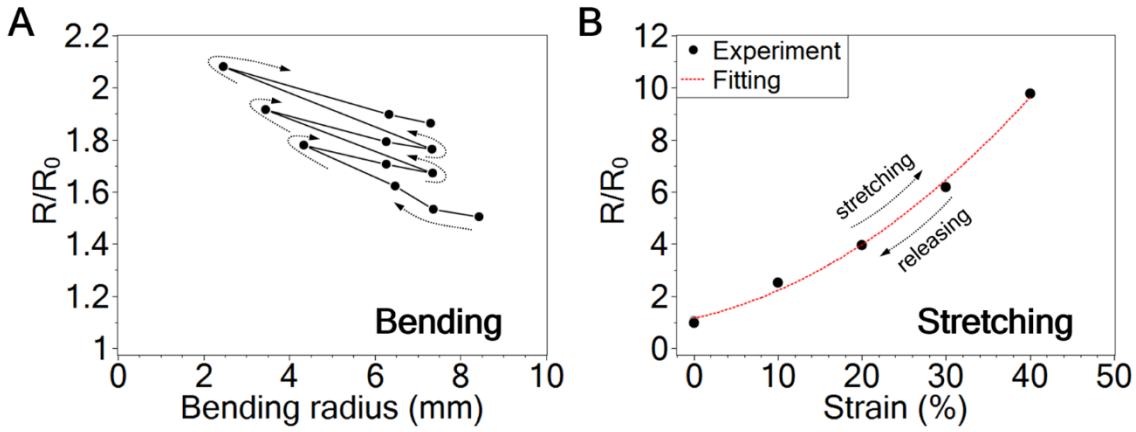

fig. S11. Normalized resistance for bending and stretching. (**A**) Normalized resistance (R/R_0) versus bending radius for MXene multilayers on PET for multiple stages of bending at radii ranging from 8.4 mm to 2.5 mm. The resistance is normalized against the resistance of the flattened sample. (**B**) Normalized resistance versus strain for MXene multilayers on PDMS for multiple stages of tensile strain. R_0 = 22.4 kΩ (bending) and 1.66 MΩ (stretching).

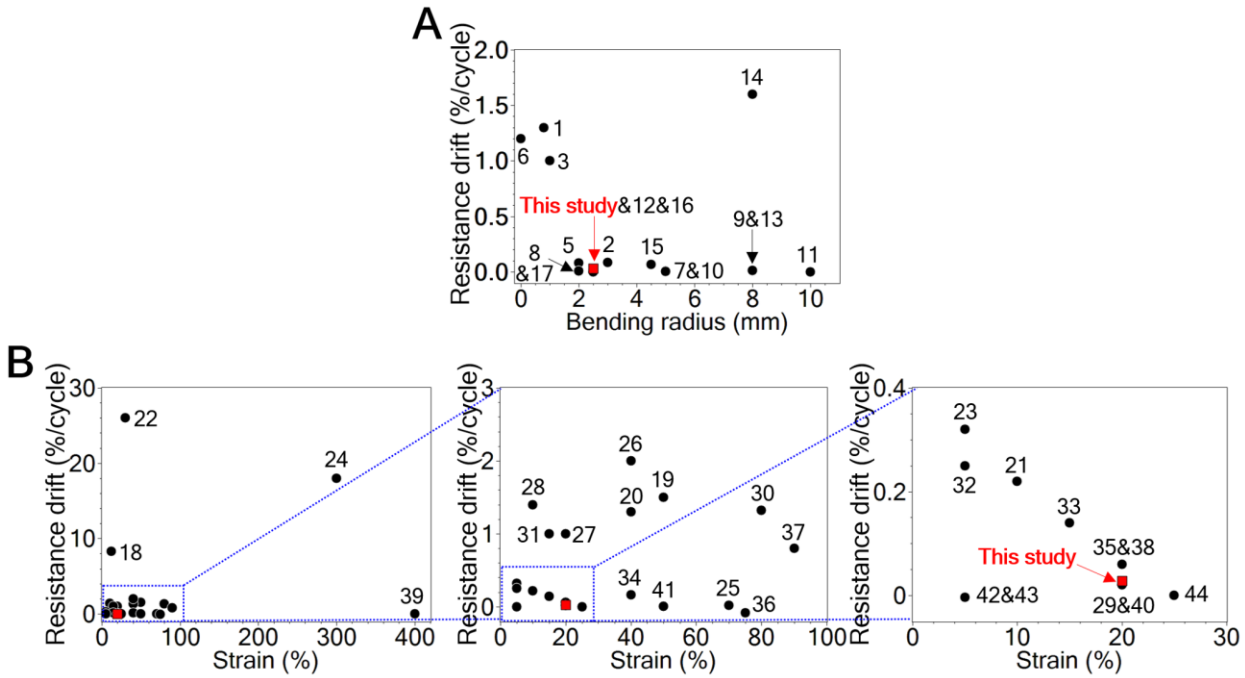

fig. S12. Comparison of resistance drift in literature. (A) Comparison of resistance drift between the bendable MXene coatings herein and other bendable conductors. (B) Comparison of resistance drift between the stretchable MXene coatings and other stretchable conductors.

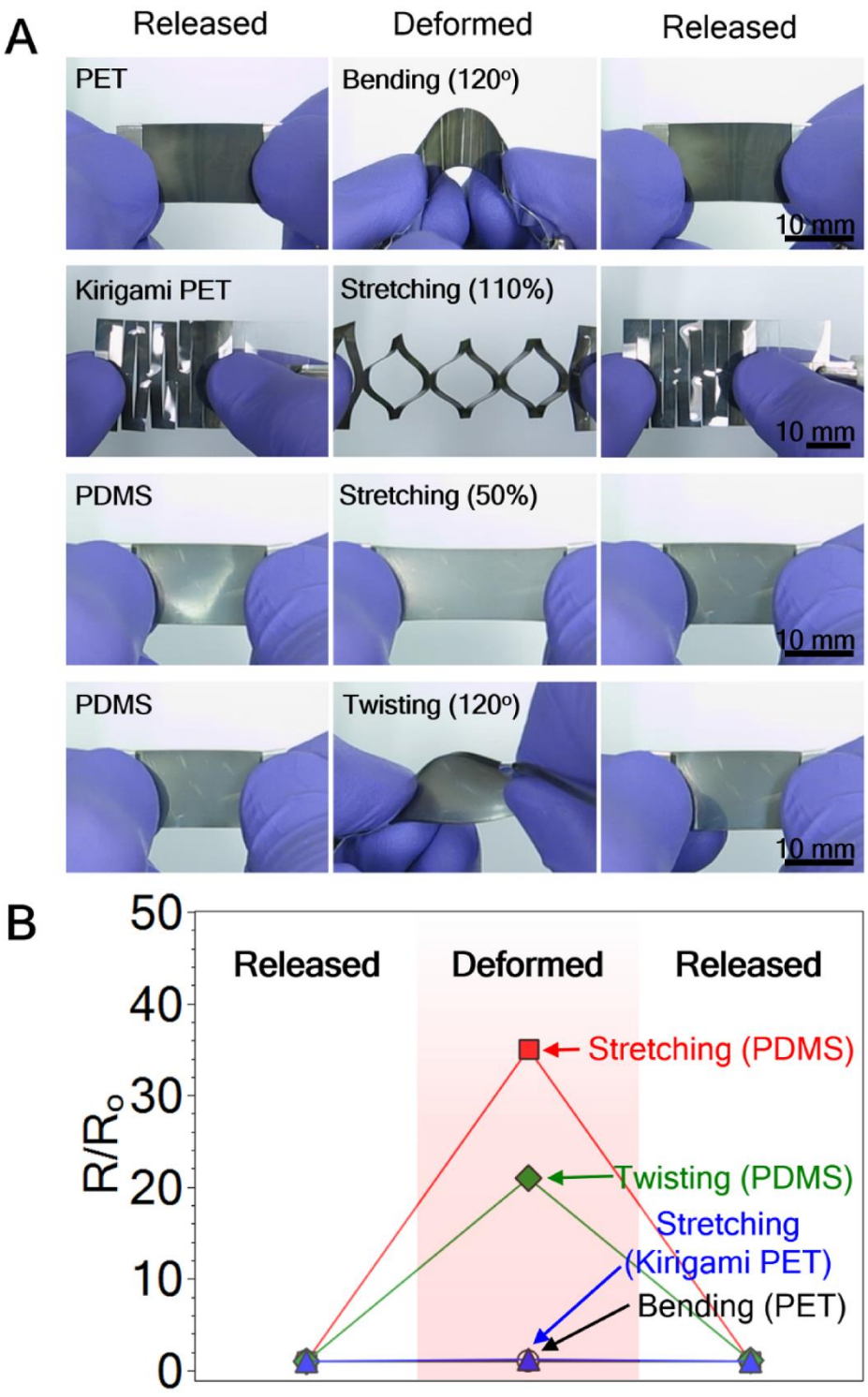

fig. S13. Images and normalized resistance of MXene multilayers on a variety of substrates. (**A**) Digital images and (**B**) normalized resistance (R/R_0) of MXene multilayers on PET, kirigami patterned PET, and PDMS under bending, stretching, and twisting. All samples were pre-deformed.

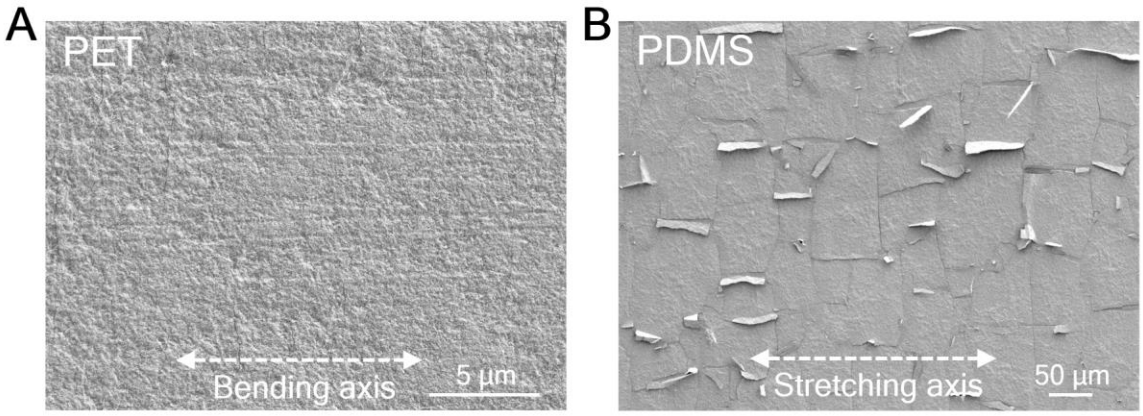

fig. S14. SEM images of MXene multilayers after bending and stretching. Low-magnification SEM images of deformed MXene multilayers on (**A**) PET and (**B**) PDMS after bending (r = 4.4 mm) and stretching (ε = 20 %), respectively.

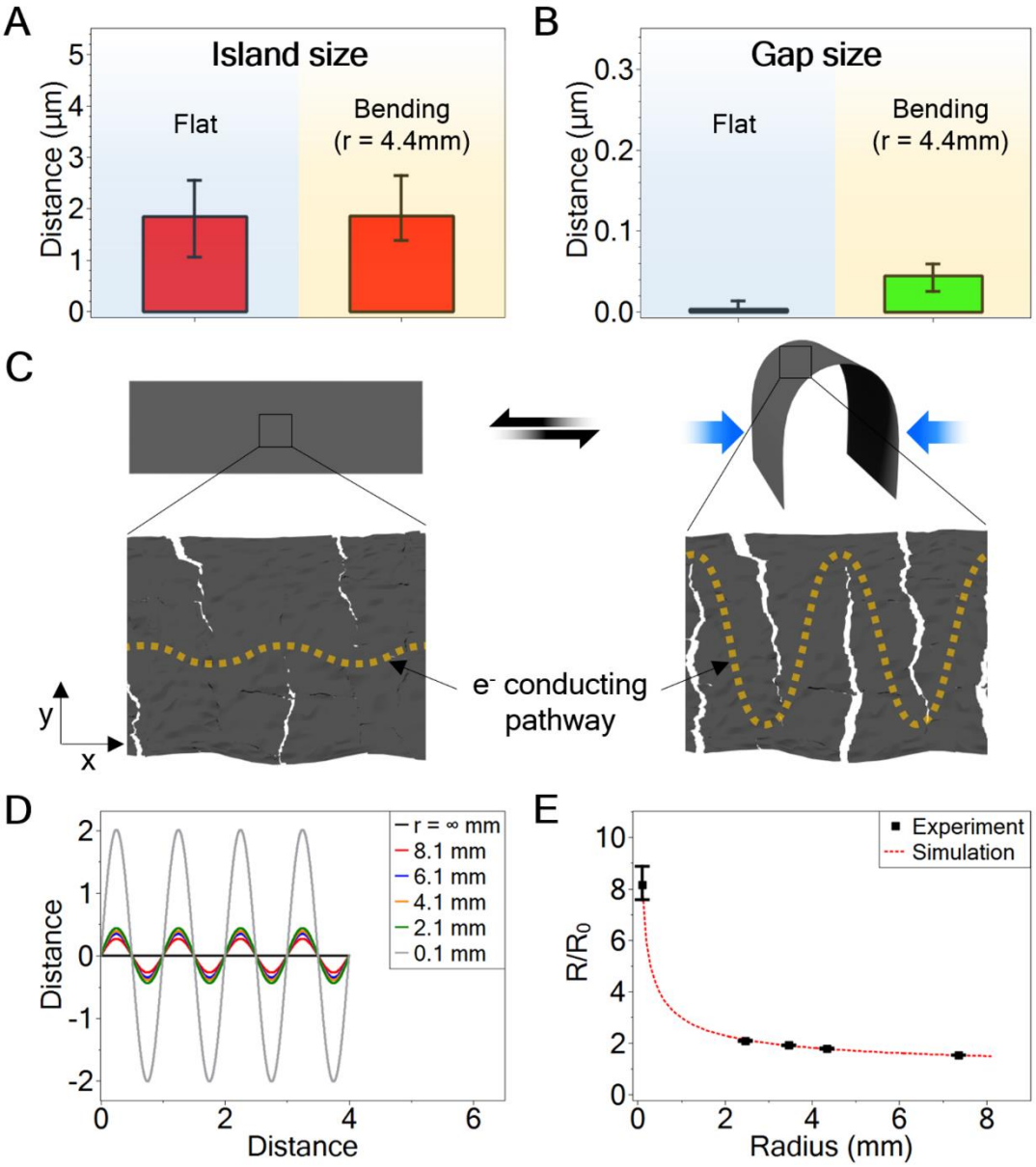

fig. S15. Geometric analysis of defects in bending. Average size of (**A**) islands and (**B**) gaps. (**C**) Schematic illustrations showing the mechanism of electromechanical behavior under bending. (**D**) Simulation results of the sinusoidal model. (**E**) Response of the multilayer to the applied bending by experimental measurement and numerical model. A geometric analysis (*23*) revealed that an electron conduction path becomes more tortuous with strain because of the gap creations. We assume that the gaps are created periodically, the length of the gaps increase with bending, and the tortuous path resembles a sine wave. Thus, with assumption that resistivity (ρ) and cross-sectional area (a) are constant, resistance can be expressed by

$$R = \frac{\rho l}{a} \propto l(r) = \int \sqrt{1 + \left(\frac{dx}{dy}\right)^2}\, dx \qquad \text{(a)}$$

$$y = A\sin(Bx) \quad \text{(b)}$$

where ε is strain; x is variable; A is an amplitude which is a function of bending radius, $f(r)$; and B is a constant (i.e., 2π). Physically, an amplitude should increase with bending. A can be determined by fitting to experimental data (fig. S15D).

$$A = 0.6854\, r^{0.4661} \quad \text{(c)}$$

Thus, by knowing A, equation y is shown to follow a power-law

$$y = A\sin(Bx) = 0.6854\, r^{0.4661}\sin(2\pi x) \quad \text{(d)}$$

Because equation (a) does not have an analytical solution, it should be solved numerically. The numerical solution of l and relative resistance are below

$$l = l_o 3.0537 r^{0.365} \quad \text{(e)}$$

$$\frac{R}{R_o} = \frac{l}{l_o} = 3.0537 r^{0.365} \quad \text{(f)}$$

where l_o is the initial length of the film, and R_o is the initial resistance. The excellent agreement between the model and experiment (fig. S15E) allows us to gauge the resistance dependence on bending radius.

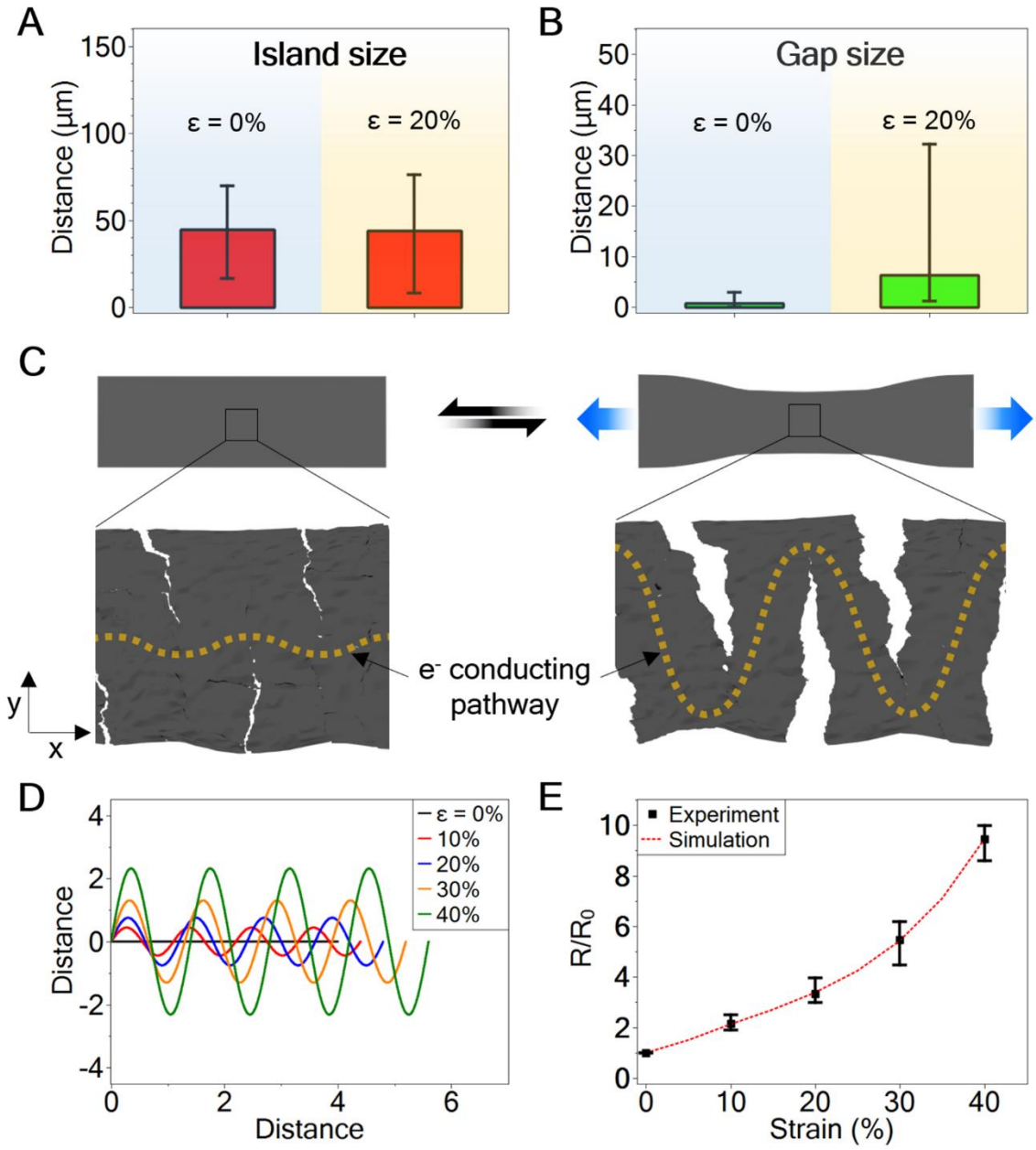

fig. S16. Geometric analysis of defects in stretching. Average size of (**A**) islands and (**B**) gaps. (**C**) Schematic illustrations showing the mechanism of electromechanical behaviors under tensile strain (stretching). (**D**) Simulation results of the sinusoidal model. (**E**) Response of the multilayer to the applied strain by experimental measurement and numerical model. A geometric analysis (*23*) reveals that the conductive path becomes more tortuous with strain because of the creation of gaps and islands. We assume that the gaps are created periodically, the length of the gaps increase with strain, and the tortuous path resembles a sine wave. Thus, with assumption that resistivity (ρ) and cross-sectional area (a) are constant, resistance can be expressed by

$$R = \frac{\rho l}{a} \propto l(\varepsilon) = \int \sqrt{1 + \left(\frac{dx}{dy}\right)^2}\, dx \qquad \text{(g)}$$

$$y = A\sin(Bx) \quad \text{(h)}$$

where ε is strain; x is variable; A is an amplitude which is a function of strain, $f(\varepsilon)$; and B is a function of strain, $f(\varepsilon) = 2\pi/(1+\varepsilon)$.

The amplitude and a period should increase with strain. A can be determined by fitting to experimental data (fig. S16D).

$$A = 49.7\varepsilon^3 - 20.0\varepsilon^2 + 5.8\varepsilon \quad \text{(i)}$$

Thus, by knowing A, equation y is shown to increase with strain

$$y = A\sin(Bx) = (49.7\varepsilon^3 - 20.0\varepsilon^2 + 5.8\varepsilon)\sin((\frac{2\pi}{1+\varepsilon})x) \quad \text{(j)}$$

Because equation (g) does not have an analytical solution, it should be solved numerically. The numerical solution of l and relative resistance are below

$$l = l_o 1.1032\exp(5.4223\varepsilon) \quad \text{(k)}$$

$$\frac{R}{R_o} = \frac{l}{l_o} = 1.1032\exp(5.4223\varepsilon) \quad \text{(l)}$$

where l_o is the initial length of film, and R_o is an initial resistance. The excellent agreement between the model and experiment (fig. S16E) allows us to gauge the resistance dependence on strain.

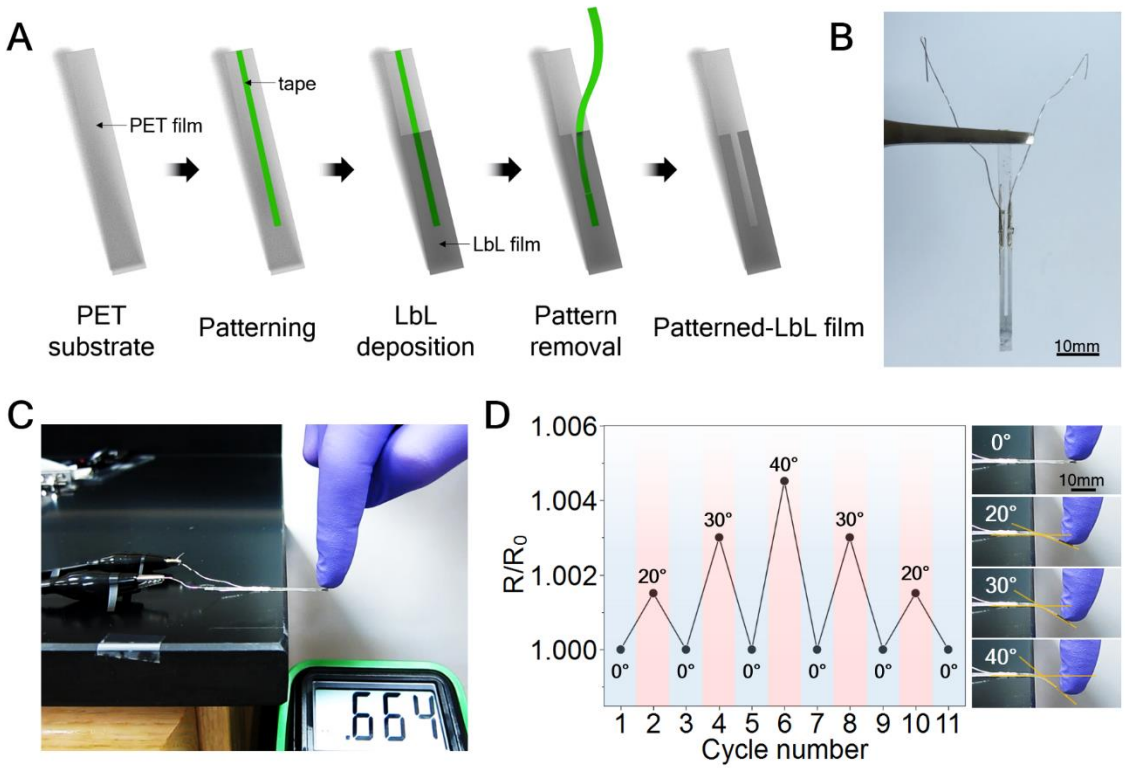

fig. S17. A multilayer strain sensor. (A) An illustration showing the fabrication of a patterned MXene multilayer strain sensor. (B) A digital image of the patterned MXene multilayer strain sensor with copper wire connections and silver paste. (C) A digital image of electromechanical testing. (D) Normalized resistance (R/R_0) *vs.* bending angle. R_0 = 664 kΩ.

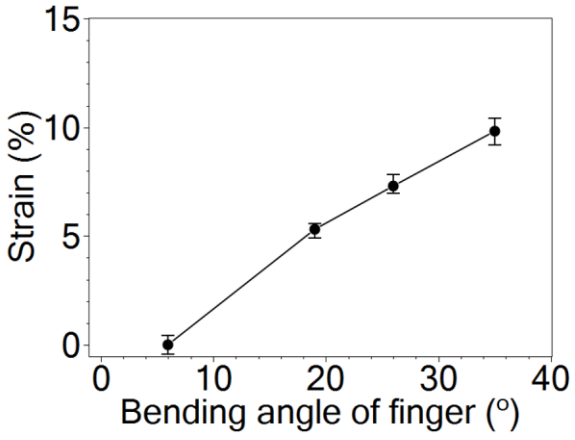

fig. S18. Strain versus the angle at the index finger. The strain sensor was attached to an index finger and bent at various angles.

table S1. Atomic composition at the surface of cast MXene sheets, $(PDAC/MXene)_{20}$ multilayer terminated with MXene, and $(PDAC/MXene)_{20.5}$ multilayer terminated with PDAC from XPS survey spectra (fig. S8). Calculated atomic composition of MXene multilayers obtained using both QCM and XPS data. We assume that atomic ratio of C and N of PDAC is 8:1.

	MXene	$(PDAC/MXene)_{20}$ finished with MXene	$(PDAC/MXene)_{20.5}$ finished with PDAC	Calculated (PDAC/MXene = 10:90 w/w)
C	44.5	58.1	64.0	51.7
Ti	22.8	18.0	12.6	19.0
O	25.3	20.0	18.6	21.1
F	6.9	3.0	1.8	5.8
N	0.6	0.9	3.1	2.3

Both $(PDAC/MXene)_{20}$ and $(PDAC/MXene)_{20.5}$ multilayers have higher carbon content than that of MXene due to presence of PDAC. We calculated atomic ratio of PDAC/MXene (=10:90 w/w) composite using QCM and XPS data. We assume that atomic ratio of C and N of PDAC is 8:1. The calculation result is in good agreement with XPS data.

table S2. Characteristics of flexible MXene-based films or coatings.

Sample[a)]	Substrate	Preparation method	Max. strain [%]	Max. bending radius [mm]	Sheet resistance[b)] [kΩ/sq]	Conduc-tivity [S/m]	Flexure type	Ref.
MXene	- (free-standing)	Vacuum-assisted filtration	1	-	1×10^{-3}	2×10^{5}	Rolling /folding	(*8*)
MXene/PVA = 90:10	- (free-standing)	Vacuum-assisted filtration	2	-	1×10^{-2}	2×10^{4}	Rolling /folding	(*8*)
MXene/PVA = 40:60	- (free-standing)	Vacuum-assisted filtration	4	-	2×10^{3}	4×10^{-2}	Rolling /folding	(*8*)
MXene/ polyacrylamide = 75:25	- (free-standing)	Casting	-	-	-	3×10^{0}	N/A	(*9*)
MXene/PAM = 31:69	- (free-standing)	Casting	-	-	-	1×10^{0}	N/A	(*9*)
MXene	- (free-standing)	Vacuum-assisted filtration	-	-	4×10^{-2}	1×10^{4}	Rolling	(*30*)
Mixed MXene/SWCNT = 50:50	- (free-standing)	Vacuum-assisted filtration	-	-	2×10^{-2}	3×10^{4}	Rolling	(*30*)
Sandwich-like MXene/SWCNT = 50:50	- (free-standing)	Vacuum-assisted filtration	-	-	1×10^{-2}	4×10^{4}	Rolling	(*30*)
Mixed MXene/MWCNT = 50:50	- (free-standing)	Vacuum-assisted filtration	-	-	3×10^{-2}	2×10^{4}	Rolling	(*30*)
Sandwich-like MXene/MWCNT = 50:50	- (free-standing)	Vacuum-assisted filtration	-	-	2×10^{-2}	2×10^{4}	Rolling	(*30*)
Sandwich-like MXene/onion-like carbon = 50:50	- (free-standing)	Vacuum-assisted filtration	-	-	6×10^{-2}	1×10^{4}	Rolling	(*30*)
Sandwich-like MXene/reduced graphene oxide = 50:50	- (free-standing)	Vacuum-assisted filtration	-	-	1×10^{-2}	4×10^{4}	Rolling	(*30*)
MXene[b)]	Polyester	Spray Coating	-	3.8	$1\sim8\times10^{0}$	6×10^{3}	Bending	(*20*)
MXene	Polyether-imide	Spin coating	-	5.1	1×10^{0}	7×10^{5}	Bending	(*31*)
MXene/PDAC multilayers = 90:10 (This study)	PDMS[c)]	Layer-by-layer coating	50	-	5×10^{0}	2×10^{3}	Stretching	This study

MXene/PDAC multilayers = 90:10 (This study)	PET[d)]	Layer-by-layer coating	-	2.5	5×10^{0}	2×10^{3}	Bending	This study

[a)]Based on weight ratio; [b)]Sheet resistance was calculated using Sheet resisatance [ohm sq^{-1}] = 1/(conductivity [S m^{-1}] × thickness [m]) where sq is unitless; [c)]Polyethylene terephthalate; and [d)]Polydimethylsiloxane.

table S3. Characteristics of reported bendable conductors.

No.	Sample	Sub-strate	Preparation method	Max. bending radius [mm]	Sheet resistance[a] [kΩ/sq]	Con-ductivity [S/m]	Cycle num-ber	Cycle bending radius [mm]	Resistance change per cycle [%/cycle]	Ref.
This study	MXene/PDAC	PET	Layer-by-layer coating	2.5	5	2×10^3	2000	2.5	0.05	This study
1	Graphene foams/PDMS	-	Template-directed CVD	0.8	-	1×10^3	10	0.8	1.3	(*32*)
2	Graphene	PMMA[b]	CVD	1.0	0.4	-	100	3.0	0.09	(*33*)
3	Graphene	PMMA	CVD	1.0	0.4	-	100	1.0	1	(*33*)
4	MWCNT/reduced graphene oxide	PET	Layer-by-layer coatings	90° bending angle	60	-	100	90° bending angle	-	(*34*)
5	Glassy graphene	PDMS	Laser direct writing method	2.0	1	1×10^4	250	2.0	0.08	(*35*)
6	Ag nanowire /PVA[c]	PET	Wet-chemical fabrication	0.0	0.003~0.2	-	250	0	1.2	(*34*)
7	Ag nanowire /graphene	PET	Vacuum filtration	5.0	0.0001~3	1×10^5	500	5.0	0.01	(*15*)
8	Graphene/Ag nanowire foam/PDMS	-	Polymer-assisted assembly /PDMS infiltration	2.0	-	1×10^3	500	2.0	0.005	(*36*)
9	PEDOT:PSS /graphene oxide	PEN[o]	Spin-coating	8.0	0.1	8×10^4	1000	8.0	0.01	(*37*)
10	PEDOT:PSS /graphene oxide	PET	Spin-coating	5.0	~0.1	-	1000	5.0	0.005	(*38*)
11	PEDOT:PSS	PET	Spin-coating	10.0	0.4	-	2000	10.0	-0.0005	(*39*)
12	Ag nanowire	PET	Transfer onto PET	2.5	0.01	1×10^6	2000	2.5	0.013	(*40*)
13	PEDOT:PSS	PET	Spin-coating	8.0	0.5	1×10^5	2500	8.0	0.012	(*41*)
14	Indium tin oxide (ITO)	PET	CVD	8.0	0.01	1×10^5	2500	8.0	1.6	(*41*)
15	Ag particle attached MWCNT	PET	Drop-casting	4.5	0.3	3×10^6	3000	4.5	0.07	(*42*)
16	Graphene foams/PDMS	-	Template-directed CVD	2.5	-	1×10^3	10000	2.5	0.0003	(*32*)
17	Graphene oxide /Ag nanowire	PET	Bar- or spray-coating	2.0	0.03	-	10000	2.0	0.007	(*43*)

[a]Conductivity was calculated using Conductivity [$S\ m^{-1}$] = 1/(sheet resistance [$ohm\ sq^{-1}$] × thickness [m]) where sq is unitless; [b]PMMA: poly(methyl methacrylate); and [c]PVA: poly(vinyl alcohol); and [o]PEN: poly(ethylene naphthalate).

table S4. Characteristics of reported stretchable conductors.

No.	Sample	Sub-strate	Preparation method	Max. strain [%]	Sheet resis-tance[a] [kΩ/sq]	Con-ductivity [S/m]	Cycle num-ber	Cycle strain [%]	Resistance change per cycle [%/cycle]	Ref.
This study	MXene/PDAC[b]	PDMS[c]	Layer-by-layer coating	50	5	2×10^3	2000	20%	0.03	This study
18	Graphene	PDMS or PET[d]	CVD[e] method /transfer	30	~1	-	3	12%	8.3	(*44*)
19	Graphene foams/PDMS	-	Template-directed CVD	100	-	$\sim1\times10^3$	10	50%	1.5	(*32*)
20	CNT /dimethacrylate crosspolymer	Dimeth-acrylate cross-polymer	Photo-crosslinked polymeri-zation	50	0.2	-	14	40%	1.3	(*45*)
21	3D PEDOT:PSS[f] aerogel/PDMS	-	Aerogel embedment into PDMS	43	0.002	-	15	10%	0.2	(*46*)
22	Graphene/ polyurethane	-	Compression molding	300	2000	1×10^{-3}	20	30%	26	(*47*)
23	Graphene/ polyurethane	-	Compression molding	300	2000	1×10^{-3}	100	5%	0.3	(*47*)
24	Carbon nanofiber /paraffin wax–polyolefin thermoplastic	Natural rubber	Spray coating	600	~0.1	1×10^3	50	300%	18	(*48*)
25	Cu	Pre-strained PDMS	Metal electroless deposition	100	0.16	2×10^7	50	70%	0.02	(*49*)
26	Ag nanowire /graphene oxide	PUA[g]	Solution-based coating	100	0.01	-	100	40%	2	(*50*)
27	Ag nanowire /graphene oxide	PUA	Solution-based coating	100	0.01	-	100	20%	1	(*50*)
28	Graphene /PEDOT:PSS	Cotton fabrics	Spray coating	45	0.06	~100	100	10%	1.4	(*51*)
29	MWCNT[h] /Polyurethane (PU)	PU	Drop-casting	1400	-	~100	100	20%	0.06	(*52*)
30	MWCNT /Polyurethane (PU)	PU	Drop-casting	1400	-	50-100	100	80%	1.3	(*52*)
31	Positively- and negatively-charged SWCNT[i]s	PDMS	Layer-by-layer coating	80	0.6	-	100	15%	1	(*53*)
32	Graphene/ polyvinyl alcohol	-	Bidirectional freezing method	8.2	-	~250	100	5%	0.3	(*54*)
33	Super-aligned CNT/PDMS	PDMS	Embedding method	30	-	6×10^3	200	15%	0.14	(*55*)
34	Graphene/Ag nanowire/PDMS	-	Polymer-assisted assembly /PDMS infiltration	40	-	1×10^3	500	40%	0.16	(*36*)
35	Graphene/Ag nanowire/PDMS	-	Polymer-assisted assembly /PDMS infiltration	40	-	1×10^3	500	20%	0.06	(*36*)

36	Graphene/natural rubber	natural rubber	Solution-based coating	~800	-	~0.1	920	75%	-0.08	(*56*)
37	Graphene /graphene scrolls	SEBS[j)]	CVD	100	0.1	-	1000	90%	0.8	(*57*)
38	SWCNT	PUA[k)]	Drop-casting	50	0.02	-	1000	20%	0.06	(*58*)
39	Super-aligned CNT	PDMS	Transfer onto PDMS	600	-	-	5000	400%	0.0012	(*59*)
40	Ag/MWCNT	NBR	Drop-casting	140	-	6×10^5	5000	20%	0.02	(*60*)
41	SWCNT /fluorinated copolymer	PDMS	Drop-casting	134	-	6×10^3	10000	50%	0.007	(*1*)
42	Au nanoparticle /PU	-	Layer-by-layer coating	16	-	7×10^5	10000	5%	-0.004	(*12*)
43	Au nanoparticle /PU	-	Vacuum assisted filtration	75	-	5×10^4	10000	5%	-0.003	(*12*)
44	F4TCNQ[l)]-doped SWCNT	PDMS	Spray-coating and buckling	150	0.3	1×10^5	12500	25%	0	(*61*)

[a)]Conductivity was calculated using Conductivity [S m^{-1}] = 1/(sheet resistance [ohm sq^{-1}] × thickness [m]) where sq is unitless; [b)]PDAC: poly(diallyldimethylammonium chloride); [c)]PDMS: poly(dimethylsiloxane); [d)]PET: poly(ethylene terephthalate); [e)]CVD: chemical vapor deposition; [f)]PEDOT:PSS: poly(3,4-ethylenedioxythiophene):polystyrene sulfonate; [g)]PUA: polyurethane acrylate; [h)]MWCNT: multi-walled carbon nanotubes; [i)]SWCNT: single-walled carbon nanotubes; [j)]SEBS: styrene-ethylene-butadiene-styrene; [k)]NBR: nitrile butadiene rubber; and [l)]F4TCNQ: 2,3,5,6-tetrafluoro-7,7,8,8-tetracyanoquinodimethane.

Supplementary Movie legends

movie S1. A nylon fiber coated with a MXene multilayer, showing conductive properties.

movie S2. An MXene multilayer on PET lights up a white LED under folding.

movie S3. Cyclic bending of a MXene multilayer on PET shows rapid and reversible response.

movie S4. An MXene multilayer on PET detects bending deformations.

movie S5. A kirigami MXene multilayer on PET detects stretching deformations.

movie S6. A kirigami pattern allows MXene multilayer–coated PET to be stretchable.

movie S7. An MXene multilayer on PDMS detects stretching deformations.

movie S8. An MXene multilayer on PDMS detects a twisting deformation.

movie S9. A patterned multilayer strain sensor detects various degrees of bending (0° to 40°) with rapid response. The resistance is fully recovered for bending/releasing cycles.

movie S10. A topographic scanner was fabricated using a patterned MXene multilayer–coated PET film. The MXene-coated PET bent and deformed as small objects passed through the scanner, resulting in a change in normalized resistance R/R_0.